Structure of an ultrathin aluminum oxide layer grown on a NiAl(110) substrate

T. Nishimura,[1] Y. Hoshino,[1] T. Okazawa,[2] and Y. Kido[1,*]

[1]*Department of Physics, Ritsumeikan University, Kusatsu, Shiga-ken 525-8577, Japan*
[2]*National Institute of Advanced Industrial Science and Technology, AIST Kansai, Ikeda, Osaka-fu 563-8577, Japan*

Ultrathin Al-oxide layers were grown on clean NiAl(110) substrates by a usual two-step technique and analyzed *in situ* by high-resolution medium energy ion scattering (MEIS) combined with photoelectron spectroscopy using synchrotron radiation light. It is found that the oxide layer comprises four atomic layers of alternating O/Al planes and the surface is terminated unambiguously with an oxygen layer. The MEIS spectra observed show that the oxide layer takes a four-layered structure of $O(1.35 \pm 0.07)/Al(1.2 \pm 0.05)/O(1.25 \pm 0.1)/Al(0.95 \pm 0.1)/NiAl(110)$ in unit of 10^{15} at./cm^2. This supports a reduced corundum structure rather than stoichiometric γ-Al$_2$O$_3$(111) and $k-$ Al$_2$O$_3$(001). The observed Al $2p_{1/2,3/2}$ core level spectra consist of three components with binding energies (Al $2p_{3/2}$) of 72.53, 73.55, and 74.75 eV, which are assigned to the bulk NiAl, the fourth layer Al on top of the bulk NiAl(110), and the second layer Al sandwiched between the top and third layers oxygen, respectively. The component with the highest binding energy for the as-grown (oxidized at 400 °C) film shifts to lower energy side by 0.4 eV after subsequent annealing at 900 °C, indicating that the annealed surface is reduced and the Al-O bond length is extended significantly.

The ultrathin aluminum oxide layer with good crystallinity grown on NiAl(110) has recently attracted much attention because of its wide application to heterogeneous catalysis as a stable support and of suppression of charging effects allowing a variety of analysis probes to characterize itself as well as fine metal particles on it. Up to now, there have been many reports on the structure of the aluminum oxide layer formed on NiAl(110).[1–7] Low energy electron diffraction patterns showed that the oxide layer consists of two identical domains with a large unit mesh ($a_1 = 10.55$ Å, $a_2 = 17.88$ Å) with an angle of 88.7° between the unit vectors, and the mesh is rotated by about 24° with respect to the $[1\bar{1}0]$ axis of NiAl(110).[3,4] Jaeger *et al.*[2] observed high-resolution electron energy loss spectra together with valence band and Al $2p$ core level spectra and concluded that the aluminum oxide layer on NiAl(110) was γ-Al$_2$O$_3$ rather than α-Al$_2$O$_3$. Recently, an extended surface x-ray diffraction study[8] obtained an overall bestfit by assuming a κ- Al$_2$O$_3$-like layer not α-, γ-, and τ-Al$_2$O$_3$-like layers. The κ-Al$_2$O$_3$ structure was previously predicted by an *ab initio* first principles calculations.[9] Quite recently, however, Kresse *et al.*[10] performed scanning tunneling microscope observations and finite-temperature molecular dynamics calculations based on the density functional theory and proposed a reduced corundum (0001) surface for the ultrathin aluminum oxide layer on NiAl(110). The above structure model was partly corrected and replaced by that with an antiphase domain boundary.[11] As mentioned above, the structure of the aluminum oxide layer is still a debatable issue.

In this study, we prepared the aluminum oxide layer on a clean NiAl(110) substrate by the usual two-step technique[2,3] and analyzed *in situ* by high-resolution medium energy ion scattering (MEIS) combined with photoelectron spectroscopy (PES) using synchrotron radiation (SR) light. The former determines the elemental depth profile in a layer-by-layer fashion and the latter gives the electronic states of aluminum and oxygen.[12,13] The toroidal electrostatic analyzer

(ESA) employed here has an excellent energy resolution $\Delta E/E$ (full width at half maximum) of 9×10^{-4}, which allows a layer-by-layer analysis. In order to determine the absolute amounts of O and Al, an accurate measurement of the integrated beam current is indispensable. For this purpose, a voltage of +90 V was applied to the sample and the beam current was conducted to ground via an ammeter. The effect of radiation damage induced by ion impact was suppressed by shifting the incident beam position slightly after an integrated beam current of 1 μC. In the PES experiment, we calibrated the incident photon energy using second harmonic waves and analyzed the energy of emitted photoelectrons by a hemispherical ESA.

Clean NiAl(110) surfaces were obtained by repetition of sputtering by 0.75 keV Ar$^+$ bombardment followed by annealing at 900 °C for 10 min in ultrahigh vacuum (UHV: $\sim 1 \times 10^{-10}$ Torr). Reflection high energy electron diffraction (RHEED) observation showed clear (1×1) patterns with sharp Kikuchi lines. Then we measured the MEIS and PES spectra using 120 keV He$^+$ ions and 120 and 240 eV SR photons, respectively, and confirmed the clean surfaces without any contaminations. The ultrathin aluminum oxide layer was grown on the clean NiAl(110) surface by the two-step process, namely, first oxidized at 400 °C for 40 min at an O$_2$ pressure of 5×10^{-7} Torr (1200 L) and then annealed at 900 °C for 120 min in UHV. The RHEED pattern observed for the as-grown sample shows the weak spots from the NiAl(110) substrate and broad and fuzzy lines from aluminum oxide, indicating growth of very fine or less-ordered aluminum oxide domains. The RHEED images observed at [100] and [110] azimuth for the annealed sample are well reproduced assuming a rhomboidal unit cell ($a_1 = 10.8$ Å, $a_2 = 18.0$ Å, $\alpha = 87.7°$) with an angle of 24.7° between the longer translation vector $\vec{a}_2$ and the [110] axis of NiAl(110). This is well consistent with that ($a_1 = 10.55$ Å, $a_2 = 17.89$ Å, $\alpha = 88.6°$) reported previously.[3,14]

First, we performed high-resolution MEIS analysis for the annealed sample using 125 keV H$^+$ and 120 keV He$^+$ ions. It

is crucial for precise MEIS analysis to know the stopping powers, energy straggling, and He⁺ fractions dependent on emerging angle, the ion velocity, and the surface elements.[15,16] The scattering yield $Y_a(n)$ from atoms a in an nth atomic layer is given by

$$Y_a(n) = Q \left(\frac{d\sigma}{d\Omega} \right)_a A_a(n) \Delta\Omega \cdot \varepsilon \, \eta_+, \qquad (1)$$

where Q, $(d\sigma/d\Omega)_a$, $A_a(n)$, and $\Delta\Omega$ are integrated beam current, differential scattering cross section, areal density of atoms a in the nth atomic layer, and the solid angle subtended by the detector, respectively. The detection efficiency ε of the microchannel plate/position sensitive detector system of the toroidal ESA was estimated previously to be 0.44 using a surface-barrier type solid state detector. The solid angle $\Delta\Omega$ is exactly known (7.64×10^{-5}) and $(d\sigma/d\Omega)_a$ is calculated numerically using the ZBL potential.[17] The stopping powers of O and Ni were determined previously to be $1.1 \times S_Z(\text{O})$ and $1.0 \times S_Z(\text{Ni})$, respectively, where S_Z denotes the Ziegler's stopping powers for He ions.[17] Basically, we used Ziegler's stopping powers for both H⁺ and He⁺ ions and the Lindhard-Scharff formula[18] for energy straggling. Surface stopping powers and straggling were taken into account by expanding the stopping region toward the vacuum side by a half-inter planar distance.[19] The most important factor dominating the accuracy of the present MEIS analysis is the H⁺ and He⁺ fractions (η_+), which depend on emerging ion energy and also on emerging angle and the atomic species of the top layer. We used the H⁺ and He⁺ fractions for the scattering component from the top layer of O determined for Ni(111)-2×2-O (Ref. 20) and TiO₂(110)-1×1 whose surfaces are terminated with an O layer having areal densities of 4.65×10^{14} and 1.56×10^{15} at./cm². Another factor contributing to elemental depth profiling by MEIS is a spectrum asymmetry induced by inner shell excitations during a large-angle collision.[21] According to the formulation by Grande *et al.*,[21] we assumed the following exponentially modified Gaussian function,

$$f(\Delta E) = \frac{\alpha}{2} \exp\left[-\frac{\alpha}{2}(2\Delta E - \sigma^2 \alpha) \right] \left[1 + \text{erf}\left(\frac{\Delta E - \sigma^2 \alpha}{\sqrt{2}\sigma} \right) \right], \qquad (2)$$

where σ, α, and $\text{erf}(x)$ are the experimental resolution (standard deviation), standard deviation for the electronic energy loss distribution, and error function, respectively. We estimated in advance the α values as a fitting parameter in the MEIS spectrum analysis for Ni(111)-2×2-O, TiO₂(110)-1×1, Si(111)-√3×√3-Sb, Ni(111), and Au(0.25–0.45 ML)/Ni(111).

Figure 1(a) shows the MEIS spectra observed for 125.4 keV H⁺ ions incident along the [100] axis of NiAl(001) and backscattering to 79.5° with respect to the surface normal. The [100] channeling incidence suppressed the scattering component from deeper layers of NiAl(110) and the large emerging angle improved the depth resolution. The energy positions for H⁺ ions scattered from O, Al, and Ni atoms assumed to be located in the top layer are
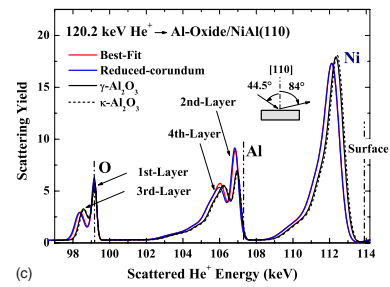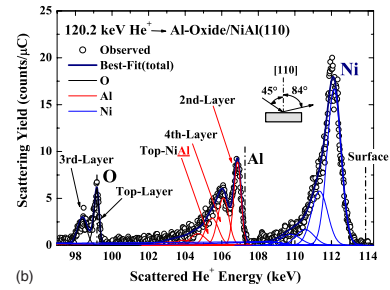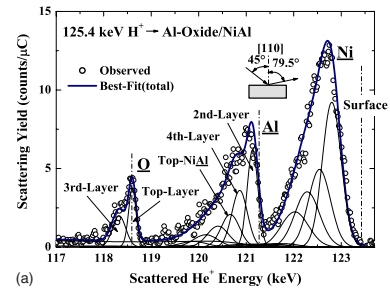

FIG. 1. (Color online) (a) MEIS spectrum (open circles) observed for 125.4 keV H⁺ ions incident along [100] axis of NiAl(110) and backscattered to 79.5° with respect to surface normal. Best-fit spectrum (solid curves) obtained assuming O(1.35 ± 0.1)/Al(1.2 ± 0.1)/O(1.25 ± 0.15)/Al(1.0 ± 0.2) on NiAl(110) in unit of 10^{15} at./cm². (b) MEIS spectrum observed for 120.2 keV He⁺ ions incident along [100] axis and backscattered to 84.0°. Best fit (solid curves) is obtained assuming stacking sequence of O(1.35 ± 0.07)/Al(1.2 ± 0.05)/O(1.25 ± 0.1)/Al(0.95 ± 0.1)/NiAl(110). (c) MEIS spectra simulated assuming stacking sequences of (i) best-fit-MEIS (red curve), O(1.35)/Al(1.2)/O(1.25)/Al(0.95); (ii) reduced corundum (Refs. 10 and 11) (blue curve), O(1.42)/Al(1.25)/O(1.25)/Al(0.85); (iii) γ alumina (Refs. 2 and 5) (black solid curve), O(1.26)/Al(0.85)/O(1.26)/Al(0.85); (iv) κ alumina (Refs. 8 and 9) (black dashed curve), O(1.21)/Al(0.81)/O(1.21)/Al(0.81).

indicated with the dotted-and-dashed straight bars. The present MEIS analysis shows unambiguously that the surface is terminated with an O layer and the ultrathin Al oxide layer takes a stacking sequence of O(1.35 ± 0.1)/Al(1.2 ± 0.1)/O(1.25 ± 0.15)/Al(1.0 ± 0.2) on NiAl(110) (in unit of 10^{15} at./cm²). Here, we used Ziegler's stopping powers and the H⁺ fraction of 0.86 ± 0.01 derived for the scattering component from the top-layer O of Ni(111)-2×2-O and of TiO₂(110)-1×1. Note that the stopping power is intimately related to the large emerging angle and thus the uncertainties of the stopping powers depend on the inaccuracy of the emerging angle. The MEIS spectrum
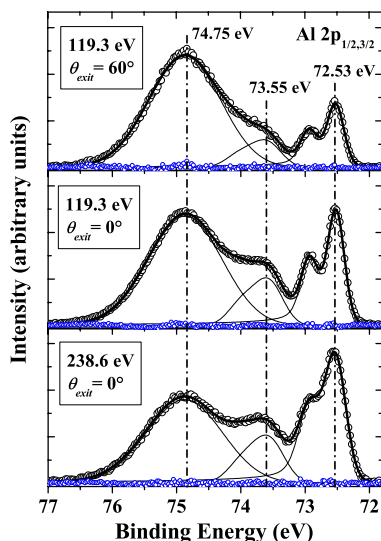
FIG. 2. (Color online) Al $2p_{1/2,3/2}$ core level spectra observed for annealed sample at photon energy of 119.3 eV (top, emission angle of 60°; middle, normal emission) and 238.6 eV (bottom, normal emission). From the bottom to the top, the spectra become more surface sensitive. The blue circles denote the difference spectrum obtained by subtracting the best-fit total spectrum from the observed one.
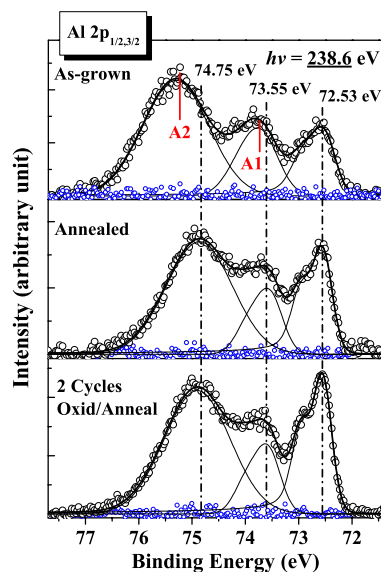

FIG. 3. (Color online) Al $2p_{1/2,3/2}$ core level spectra observed at photon energy of 238.8 eV for samples as grown (top), annealed (middle), and grown by two cycles of oxidation and/or annealing (bottom). Emission angle was fixed to surface normal direction. Solid curves are deconvoluted spectra with Gaussian shapes. The blue circles denote the difference spectrum obtained by subtracting the best-fit total spectrum from the observed one.

observed for the sample before annealing at 900 °C shows a similar four-layered structure but poor crystallinity. It is also found that annealing at 900 °C slightly reduces the oxygen content.

In order to improve the depth resolution, we measured the MEIS spectra for the annealed samples using 120 keV He$^+$ ions. Figure 1(b) shows the MEIS spectrum observed for 120.2 keV He$^+$ ions incident along the [100] axis and back-scattered to 84.0°. The observed MEIS spectrum is well reproduced by assuming the stacking sequence of O(1.35 ± 0.07)/Al(1.2 ± 0.05)/O(1.25 ± 0.1) /Al(0.95 ± 0.1)/NiAl(110)in unit of 10^{15} at./cm^2. Here, we employ the values of 0.43(±0.01), 0.40(±0.01), and 0.38(±0.01) for the scattering components from top-layer O, second- and fourth-layers Al, and third-layer of O, respectively. They were estimated from the layer-resolved MEIS spectra observed for the Ni(111)-2×2 and TiO$_2$(110)-1×1. It is interesting to compare the present MEIS result with the other structure models proposed so far. Figure 1(c) indicates the MEIS spectra simulated assuming the stacking sequences of (i) best-fit-MEIS: O(1.35)/Al(1.2)/O(1.25)/Al(0.95), (ii) reduced corundum:[10,11] O(1.42)/Al(1.25)/O(1.25)/Al(0.85), (iii) γ alumina:[2,5] O(1.26)/Al(0.85)/O(1.26)/Al(0.85), and (iv) κ alumina:[8,9] O(1.21)/Al(0.81)/O(1.21)/Al(0.81). Apparently, the present MEIS analysis supports the reduced corundum structure although a slight difference is seen for the fourth-later Al. In spite of O deficiency in the top layer, the epitaxial oxide layer is stable. In fact, we observed no scattering yield from ^{18}O in MEIS spectra for the sample exposed to ^{18}O$_2$ under an ultrahigh vacuum condition.

We observed the Al $2p_{1/2,3/2}$ core level spectra at photon energies of 120 and 240 eV for the annealed sample (see Fig. 2). In order to assign the oxide components, we observed the

intensity ratios of the three peaks observed at different energies, and geometries. From the bottom ($h\nu$=238.6 eV, normal emission) to the top ($h\nu$=119.3 eV; emission angle, 60°), the spectra become more surface sensitive. Here, the binding energy (E_B) is scaled from the Fermi level. Apparently, all the spectra consist of three components and the narrow peak with the lowest binding energy E_B of 72.53 eV (Al $2p_{3/2}$) comes from the bulk NiAl. The observed spectra are well deconvoluted by assuming an Al $2p$ spin-orbit splitting of 0.4 eV (Ref. 2) and symmetric Gaussian shapes with the branching ratios of 2.0 for the oxide components and 1.74 for the bulk NiAl.[22] For the Al $2p$ spectra from NiAl, we must take account of the screening response of conduction electrons and thus used the Doniach-Sunjic line shape[23] expressed by

$$f(E - E_B) = \frac{\Gamma(1 - \alpha)\cos[\pi\alpha/2 + (1 - \alpha)\tan^{-1}\{(E - E_B)/\gamma\}]}{\{(E - E_B)^2 + \gamma^2\}^{(1-\alpha)/2}},$$

(3)

where Γ is the Γ function, α=0.07, and γ=0.03 eV. As a result, the peak with the highest E_B value (74.75 eV) comes from the second-layer Al sandwiched between the top and the third layer of oxygen and that with the E_B value of 73.55 eV originates from the fourth layer of aluminum located on top of the NiAl(110). The present result coincides well with the data reported by Sandell *et al.*[24] The E_B values for Al $2p_{3/2}$ observed here are compared with other reports in Table I.

We also observed the Al $2p$ spectra for three different samples, prepared by (A) oxidation (as grown), (B) annealed at 900 °C, and (C) two cycles of oxidation and/or annealing

TABLE I. E_B values (eV) of Al $2p_{3/2}$ for NiAl(110) and Al-oxide layers grown on NiAl(110): (A) as grown (oxidized), (B) annealed, and (C) repeated twice the oxidation followed annealing.

	Present	Jaeger et al.[a]	Lay et al.[b]	Sandell et al.[c]
NiAl(110)	72.53 ± 0.05	72.68	72.8	72.55 ± 0.1
Al oxide/NiAl (A) As grown	73.7 ± 0.05		76.0	
	75.2 ± 0.05			
Al oxide/NiAl (B) Annealed	73.55 ± 0.05	73.75	76.0	73.6 ± 0.1
	74.75 ± 0.05	75.17		75.0 ± 0.1
Al oxide/NiAl (C) Two cycles of oxidation/anneal	73.55 ± 0.05			
	74.75 ± 0.05			
Al foil*	72.55 ± 0.05			
	72.8 ± 0.05			

[a]Reference 2.
[b]Reference 7.
[c]Reference 24 and 25.

(see Fig. 3). Also in this case, each spectrum consists of three components, one narrow peak from the bulk NiAl and two broad peaks from aluminum oxides. It is noteworthy that the E_B value of 75.2 ± 0.05 eV (Al $2p_{3/2}$) for the as-grown sample (A) is higher by ~0.4 eV than those for the samples (B) and (C). This indicates that the annealed surface is slightly reduced and the Al-O bond length is significantly extended. As mentioned before, the MEIS analysis shows a slight reduction of the oxygen content after annealing the as-grown sample at 900 °C. Repetition of oxidation and annealing does not change the intensity ratio of Al $2p$ for the Al-oxide layer to NiAl. We also measured the valence band

spectra at a photon energy of 40 eV (not shown here). The valence band offset derived is 4.3 ± 0.05 eV, which is in good agreement with the data of 4.5 ± 0.1 eV reported by Andersson et al.[25] and compatible with the value of ~4 eV for the reduced corundum structure calculated using the density functional theory (VASP).[11]

In summary, ultrathin Al-oxide layers were grown on clean NiAl(110) substrates by the usual two-step technique and analyzed *in situ* by high-resolution MEIS combined with PES using SR light. It is found that the oxide layer comprises four atomic layers of alternating O/Al planes and the surface is terminated with an oxygen layer. The stacking sequence determined here is $O(1.35 \pm 0.07)/Al(1.2 \pm 0.05)/O(1.25 \pm 0.1)/Al(0.95 \pm 0.1)/NiAl(110)$ in units of 10^{15} at./cm^2. The present MEIS analysis supports the reduced corundum structure, although a slight difference is seen for the fourth-layer Al. The other structure models of γ-Al$_2$O$_3$(111) and κ-Al$_2$O$_3$(100) are ruled out. We observed Al $2p_{1/2,3/2}$ spectra and found three peaks correlated with the four-layered structure and assigned them as the lowest binding energy E_B (Al $2p_{3/2}$) of 72.53 ± 0.05 eV coming from the bulk NiAl, and the E_B values of 74.75 and 73.55 eV from the second- and fourth-layer Al of the epitaxial oxide film, respectively. The valence band offset for the ultrathin oxide layer is estimated to be 4.3 eV, which is compatible with the value of ~4 eV for the reduced corundum structure calculated by density functional theory (VASP).

*FAX: +81-77-561-2657; ykido@se.ritsumei.ac.jp

[1] H. Isern and G. R. Castro, Surf. Sci. **211/212**, 8565 (1989).

[2] R. M. Jaeger et al., Surf. Sci. **259**, 235 (1991).

[3] J. Libuda et al., Surf. Sci. **318**, 61 (1994).

[4] M. Bäumer and H.-J. Freund, Prog. Surf. Sci. **61**, 127 (1999).

[5] R. Fanchy, Surf. Sci. Rep. **38**, 195 (2000).

[6] G. Ceballos et al., Chem. Phys. Lett. **359**, 41 (2002).

[7] T. T. Lay, M. Yoshitake, and W. Song, Appl. Surf. Sci. **239**, 451 (2005).

[8] A. Stierle et al., Science **303**, 1652 (2004).

[9] Y. Yourdshahyan et al., J. Am. Ceram. Soc. **82**, 1365 (1999).

[10] G. Kresse et al., Science **308**, 1440 (2005).

[11] M. Schmid et al., Phys. Rev. Lett. **97**, 046101 (2006).

[12] T. Nishimura, A. Ikeda, and Y. Kido, Rev. Sci. Instrum. **69**, 1671 (1998).

[13] Y. Kido, T. Nishimura, Y. Hoshino, and H. Namba, Nucl. Instrum. Methods Phys. Res. B **161-163**, 371 (2000).

[14] M. Kulawik et al., Phys. Rev. Lett. **91**, 256101 (2003).

[15] Y. Hoshino, S. Semba, T. Okazawa, and Y. Kido, Surf. Sci. **515**, 305 (2002).

[16] T. Okazawa, K. Shibuya, T. Nishimura, and Y. Kido, Nucl. Instrum. Methods Phys. Res. B **256**, 1 (2007).

[17] J. F. Ziegler, J. P. Biersack, and W. Littmark, *The Stopping and Range of Ions in Matter* (Pergamon, New York, 1985).

[18] J. Lindhard and M. Scharff, K. Dan. Vidensk. Selsk. Mat. Fys. Medd. **27**, 15 (1953).

[19] K. Sumitomo, T. Nishioka, A. Ikeda, and Y. Kido, Phys. Rev. B **56**, 7011 (1997).

[20] A. Eichler, F. Mittendorfer, and J. Hafner, Phys. Rev. B **62**, 4744 (2000).

[21] P. L. Grande et al., Nucl. Instrum. Methods Phys. Res. B **256**, 92 (2007).

[22] C. Biswas et al., Phys. Rev. B **67**, 165416 (2003).

[23] S. Hüfner, *Photoelectron Spectroscopy* (Springer-Verlag, New York, 1996).

[24] A. Sandell et al., J. Electron Spectrosc. Relat. Phenom. **76**, 301 (1995).

[25] S. Andersson et al., Surf. Sci. **442**, L964 (1999).